Supplementary Information: Ultrahigh accuracy imaging modality for super-localization microscopy

Jerry Chao[1,2,3], Sripad Ram[1,2,3], E. Sally Ward[2] and Raimund J. Ober[1,2,*]

[1]Department of Electrical Engineering
University of Texas at Dallas
800 W. Campbell Road
Richardson, TX 75080, U.S.A.

[2]Department of Immunology
University of Texas Southwestern Medical Center
6000 Harry Hines Boulevard
Dallas, TX 75390, U.S.A.

[*]Corresponding author. Address: Department of Electrical Engineering, University of Texas at Dallas, 800 W. Campbell Road, Richardson, TX 75080, U.S.A., Email: ober@utdallas.edu. [3]These authors contributed equally to this work.

Nature Methods: doi:10.1038/nmeth.2396

List of Figures

List of Tables

List of Notes

Nature Methods: doi:10.1038/nmeth.2396

Supplementary Figure 1

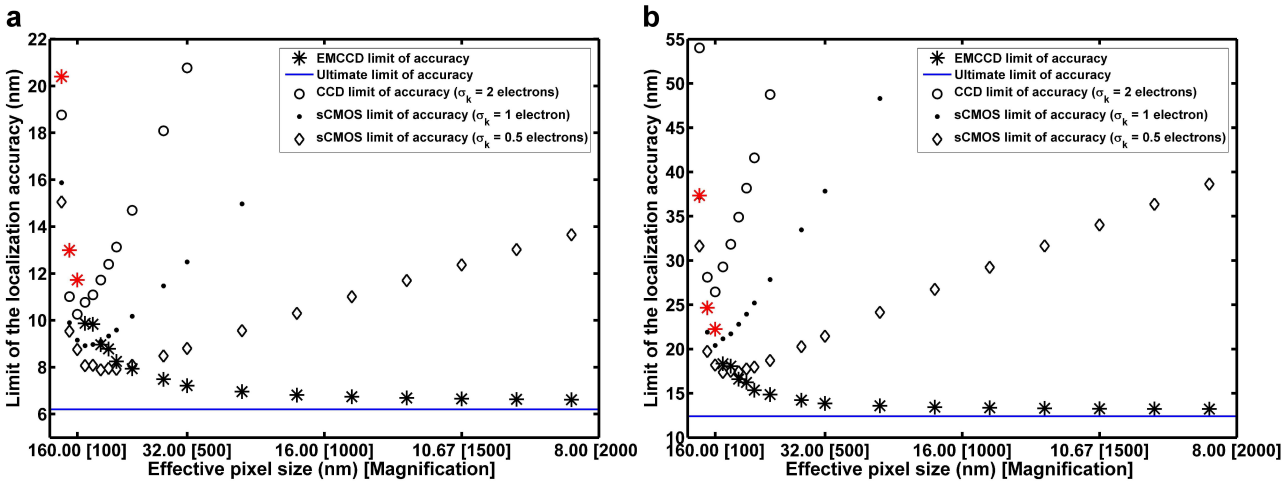

Supplementary Figure 1. Comparing EMCCD imaging with CCD/sCMOS imaging. The limits of the localization accuracy attainable with EMCCD and CCD/sCMOS imaging are shown as a function of the effective pixel size, and for an expected photon count of **(a)** $N_{photon} = 200$ and **(b)** $N_{photon} = 50$. In both **a** and **b**, the EMCCD limit of accuracy ($*$) is shown to approach the ultimate limit (blue line) with decreasing effective pixel size. The markers highlighted in red at effective pixel sizes of 373.31 nm, 224.00 nm, and 160.00 nm (or equivalently, magnifications of $M = 42.86$, 71.43, and 100, respectively) correspond approximately to standard magnifications of 40× and 63×, and exactly to the standard magnification of 100×. The CCD/sCMOS limits of accuracy are shown for a mean of $\eta_k = 0$ electrons and standard deviations of $\sigma_k = 2$ electrons ($\circ$), $\sigma_k = 1$ electron ($\cdot$), and $\sigma_k = 0.5$ electrons ($\diamond$) for the readout noise at each pixel k. All other applicable details are as given in **Supplementary Note 9** for **Figure 2b**. See also the discussion in **Supplementary Note 10**.

Nature Methods: doi:10.1038/nmeth.2396

Supplementary Figure 2

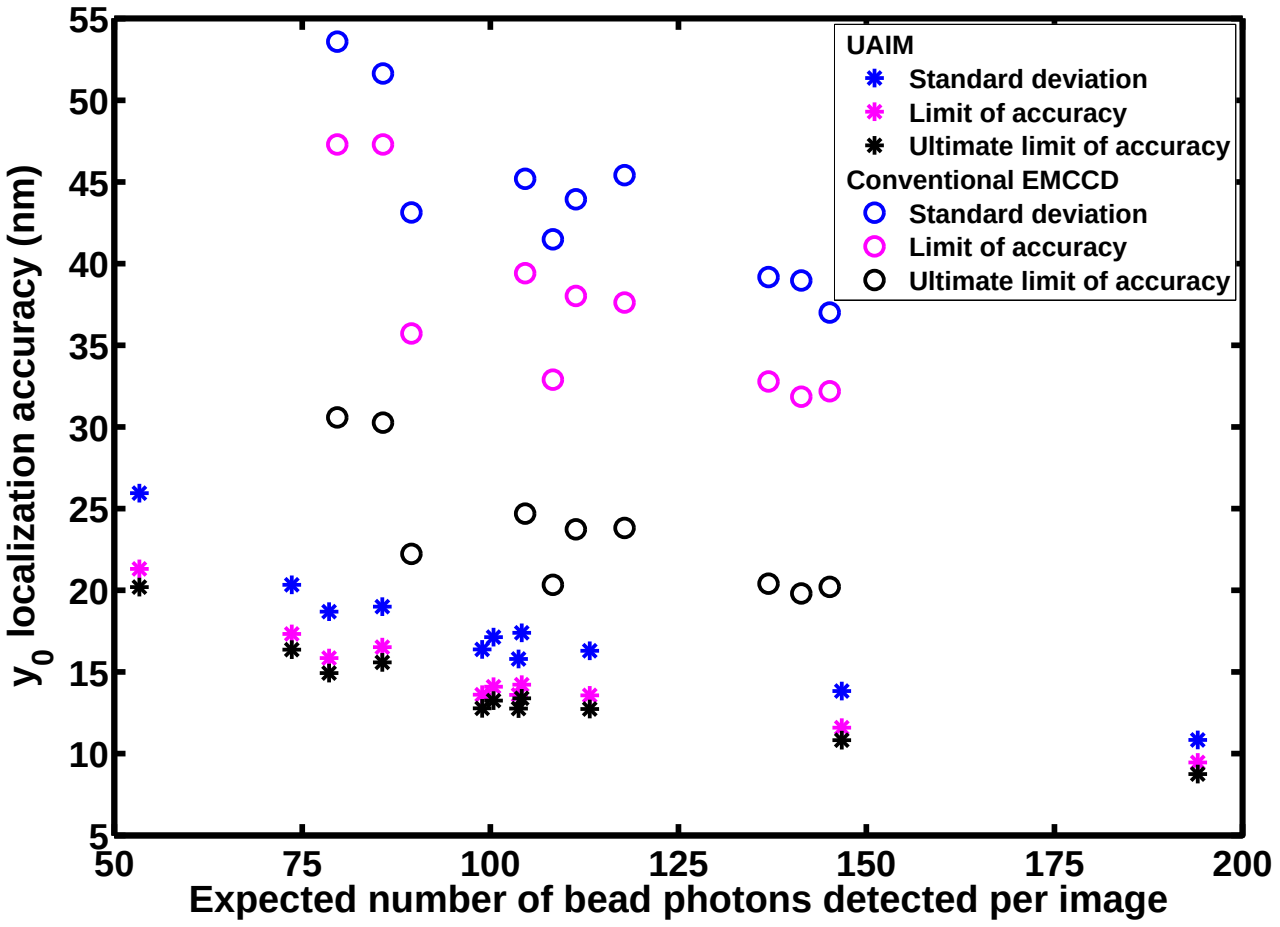

Supplementary Figure 2. Bead data analysis results for the y_0 positional coordinate. The standard deviations of the maximum likelihood estimates of the y_0 coordinate of fluorescent beads imaged using UAIM (blue $*$) and conventional EMCCD imaging (blue $\circ$) are shown. Each standard deviation corresponds to a different bead, identified by the mean number of photons detected from it per image. For each standard deviation, the corresponding limit of accuracy (magenta $*$ for UAIM, magenta $\circ$ for conventional) is shown. Likewise, the corresponding ultimate limit of accuracy (black $*$ for UAIM, black $\circ$ for conventional), which assumes an ideal detector that introduces neither noise nor pixelation, is shown. The UAIM (conventional) images were acquired with an effective pixel size of 16 nm (253.97 nm) using a 1000$\times$ (63$\times$) magnification.

Nature Methods: doi:10.1038/nmeth.2396

Supplementary Figure 3

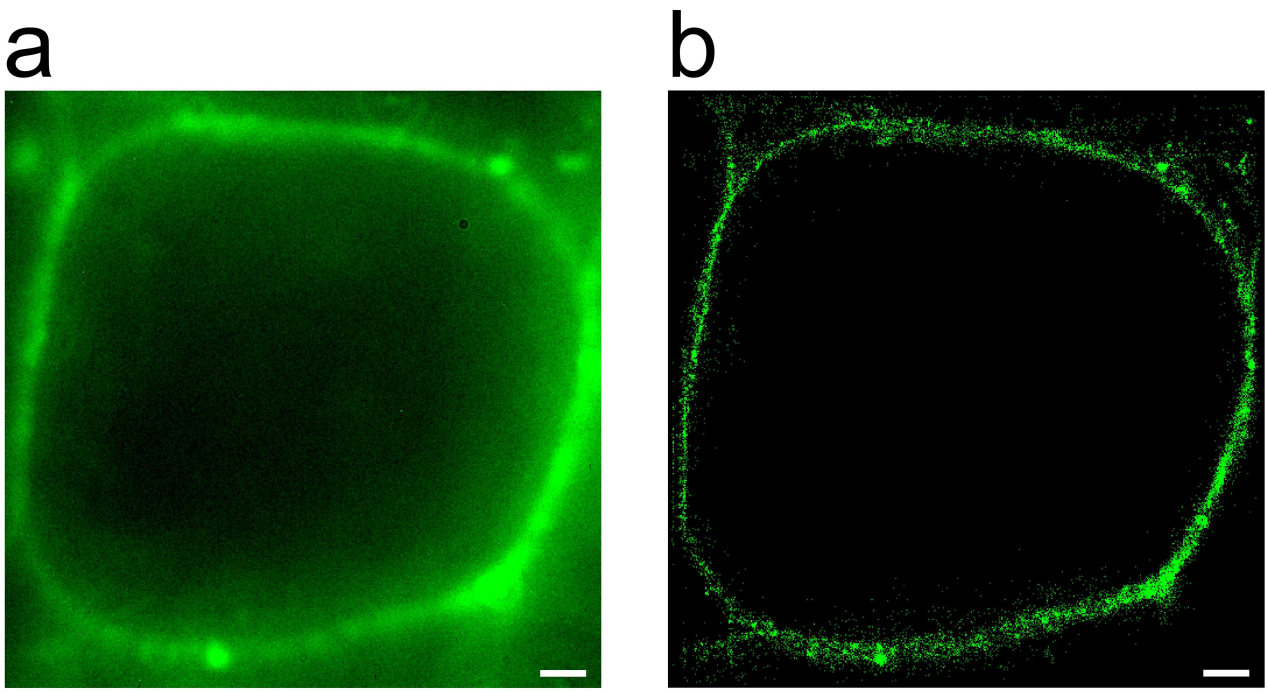

Supplementary Figure 3. Superresolution imaging of a cell membrane. **(a)** Image of the cell membrane of a Z310 rat epithelial cell, formed by summing the 4909 UAIM (630×) data images from which single Alexa647 molecules were localized to produce a superresolution image. **(b)** The superresolution image constructed from the location estimates of individual Alexa647 molecules. The average number of photons detected per molecule is 233.94. Scale bars, 1 μm.

Nature Methods: doi:10.1038/nmeth.2396

Supplementary Table 1. Accuracy of localization of single Atto647N molecules. The standard deviations of the maximum likelihood estimates of the x_0 and y_0 positional coordinates of four individual Atto647N molecules are shown with their corresponding accuracy limits and ultimate accuracy limits. Two of the four Atto647N molecules were imaged using UAIM at a 1000× magnification, and the other two were imaged using conventional EMCCD imaging at a 63× magnification. To facilitate comparison, one pair of UAIM-imaged and conventional EMCCD-imaged molecules have a similar low mean photon count, and the other pair have a similar higher mean photon count. The maximum likelihood estimation for the two UAIM-imaged (conventional EMCCD-imaged) molecules was performed on a 61×61-pixel (13×13-pixel) region of interest.

Modality	Mean photon count per image	Standard deviation of x_0, y_0 estimates (nm)	Limit of the localization accuracy for x_0, y_0 (nm)	Ultimate limit of accuracy for x_0, y_0 (nm)
UAIM	72.09	34.05, 27.05	27.90, 27.90	25.54, 25.54
Conventional EMCCD	84.00	46.21, 44.35	42.38, 41.11	25.66, 25.66
UAIM	191.35	18.82, 15.01	15.81, 15.81	14.22, 14.22
Conventional EMCCD	182.96	35.47, 36.36	32.11, 33.19	19.97, 19.97

For the maximum likelihood estimation, the width of the Airy function used to model the image of each molecule was determined to be, and set to, 0.01045 nm^{-1}, 0.00762 nm^{-1}, 0.01038 nm^{-1}, and 0.00740 nm^{-1}, respectively in the order listed from top row to bottom row. The background for each data set was likewise determined to be, and set to, 0.058, 3.38, 0.102, and 11.52 photons per pixel, respectively. See also the discussion in **Supplementary Note 5**.

Nature Methods: doi:10.1038/nmeth.2396

Supplementary Table 2. Comparison of imaging methods at different photon counts. Limits of the accuracy for localizing a point source are shown for different imaging methods and different mean photon counts N_{photon} detected from the point source. For the ultimate accuracy limit, the magnification is set to $M = 100$, and the Airy function modeling the image of the point source is centered on a 112 μm $\times$ 112 μm unpixelated region of interest. For the conventional EMCCD accuracy limit, the same magnification of $M = 100$ is used and the Airy function is centered on a region of the same size, but consisting of a 7×7 array of 16 μm $\times$ 16 μm pixels. For the UAIM and CCD accuracy limits, the specified magnification is used with a proportionally expanded array of 16 μm $\times$ 16 μm pixels. For the conventional EMCCD and UAIM scenarios, the electron multiplication gain is set to $g = 1000$, and the readout noise mean and standard deviation are respectively set to $\eta_k = 0$ electrons and $\sigma_k = 24$ electrons for each pixel k. For the CCD scenario, the readout noise mean and standard deviation are respectively set to $\eta_k = 0$ electrons and $\sigma_k = 2$ electrons for each pixel k. For all scenarios, no background component is assumed, and its mean is accordingly set to $\beta = 0$ photons for the ideal scenario, and $\beta_k = 0$ photons for each pixel k for the conventional EMCCD, UAIM, and CCD scenarios. The numerical aperture of the objective lens is set to $n_a = 1.3$, and the wavelength of the detected photons is set to $\lambda = 655$ nm. For each of the conventional EMCCD, UAIM, and CCD scenarios, the distance between its accuracy limit and the corresponding ultimate accuracy limit is expressed as a percentage (in square brackets) of the ultimate accuracy limit. The smaller this percentage, the closer the accuracy limit is to its corresponding ultimate accuracy limit.

Mean photon count	Ultimate accuracy limit (nm)	Conventional EMCCD accuracy limit (nm)	UAIM at 900× accuracy limit (nm)	UAIM at 4500× accuracy limit (nm)	CCD accuracy limit[a] (nm)
200	6.19	11.72 [89.3%]	6.81 [10.0%]	6.56 [6.0%]	10.26 [65.8%]
400	4.38	8.39 [91.6%]	4.90 [11.9%]	4.64 [5.9%]	6.77 [54.6%]
800	3.10	5.99 [93.2%]	3.56 [14.8%]	3.28 [5.8%]	4.49 [44.8%]
1600	2.19	4.26 [94.5%]	2.60 [18.7%]	2.32 [5.9%]	3.00 [37.0%]
3200	1.55	3.02 [94.8%]	1.90 [22.6%]	1.65 [6.5%]	2.01 [29.7%]

[a]Computed at near-optimal magnification (i.e., magnification that yields approximately the best localization accuracy limit) of 100×, 100×, 128.6×, 128.6×, and 185.7× for mean photon count of 200, 400, 800, 1600, and 3200, respectively. See also the discussion in **Supplementary Note 11**.

Nature Methods: doi:10.1038/nmeth.2396

Supplementary Table 3. Limits of the localization accuracy for the superresolution and live cell single molecule tracking data sets.

Experimental UAIM data set	Limit of accuracy for average molecule or image (nm)	Limit of accuracy for conventional EMCCD imaging at tenfold lower magnification (nm)	Ultimate limit of accuracy (nm)
$LAMP1^+$ structure (1000×)	24.64	34.99	22.24
Cell membrane (630×)	25.32	38.72	20.32
Atto647N tracking (1000×)	23.90	34.38	22.00

The limits of accuracy pertain to both the x_0 and y_0 coordinates, since it is assumed that the image of the dye molecule is exactly centered on the region of interest. See **Supplementary Note 15** for a description of how these limits are computed.

Nature Methods: doi:10.1038/nmeth.2396

Supplementary Note 1: UAIM's rule of thumb

The rule of thumb that the mean number of photons detected in a pixel be reduced to less than 1 is based on the pixel's *noise coefficient* (**Supplementary Note 6**) being closest to its best possible value of 1 when the condition is achieved (see **Fig. S1**). However, while it is recommended that the condition is achieved in every pixel of an image (in order to obtain as high an accuracy as possible for estimating the desired quantity), it need not be satisfied in every pixel in order for UAIM to enable estimation with an accuracy that is close to the absolute best possible. This is the meaning of the word "generally" used in describing the principle of UAIM.

Example calculations showing high estimation accuracies for scenarios where some pixels do not meet the rule of thumb of a mean photon count of less than 1 are discussed in **Supplementary Note 11** and summarized in **Supplementary Table 2**.

Supplementary Note 2: The total photon count

UAIM achieves significantly better parameter estimation accuracies than conventional EMCCD imaging by substantially lowering the mean number of photons detected in each pixel of an acquired image. This does not mean that the total number of photons detected from the object of interest should be reduced, a stipulation that would amount to a contradiction of the well-known and intuitive result that estimation accuracies can be improved by detecting more photons (i.e., collecting more data) from the object of interest[1,2]. Rather, as one can expect with conventional imaging, one can expect with UAIM that the detection of more photons from the object of interest will yield better estimation accuracies. This is in fact demonstrated by **Figure 2a** and **Supplementary Figure 2**, where for both the UAIM and the conventional data, the standard deviations of the positional coordinate estimates and the corresponding limits of accuracy can be seen to improve (i.e., decrease) with increasing numbers of photons detected per image.

In short, UAIM does not stipulate the reduction of the total number of photons detected from the object of interest. Instead, one should try to detect as many of the available photons as possible, but

Nature Methods: doi:10.1038/nmeth.2396

in a way that results in an allocation where generally less than one photon on average is detected in each pixel of the image.

Supplementary Note 3: Limits of the localization accuracy

In this paper, the standard deviation of the estimates of a positional coordinate of a simulated or experimental point source is compared with the best (i.e., smallest) possible standard deviation that is attainable in theory for the particular assumed or experimental conditions. This best possible standard deviation is referred to as the *limit of the accuracy* for estimating the positional coordinate, and it is based on the Cramer-Rao lower bound[3] from estimation theory. In this note, we give a description of how the limits of accuracy for the data models considered in this paper are calculated, and state their mathematical expressions.

Given the vector θ of parameters (i.e., quantities of interest) to be estimated, the Cramer-Rao inequality states that the covariance matrix of any unbiased estimator $\hat{\theta}$ of θ is no smaller than the inverse of the Fisher information matrix[3] $\mathbf{I}(\theta)$, i.e.,

$$\mathrm{Cov}(\hat{\theta}) \geq \mathbf{I}^{-1}(\theta). \tag{S1}$$

From equation (S1), it immediately follows that the standard deviation for estimating the jth parameter in θ can be no smaller than $\sqrt{[\mathbf{I}^{-1}(\theta)]_{jj}}$, the square root of the jth main diagonal element of $\mathbf{I}^{-1}(\theta)$. The quantity $\sqrt{[\mathbf{I}^{-1}(\theta)]_{jj}}$ is therefore the best possible standard deviation, or the limit of the accuracy, with which the jth parameter in θ can be estimated. For the localization problem considered in this paper, the parameters that are estimated are the positional coordinates x_0 and y_0 of a point source. Accordingly, the vector θ is defined to be $\theta = (x_0, y_0)$, and the quantities $\sqrt{[\mathbf{I}^{-1}(\theta)]_{11}}$ and $\sqrt{[\mathbf{I}^{-1}(\theta)]_{22}}$ are, respectively, the limits of the accuracy with which x_0 and y_0 can be estimated.

The above general result shows that the limits of accuracy are readily obtained provided that we can calculate the Fisher information matrix $\mathbf{I}(\theta)$. The precise expression for $\mathbf{I}(\theta)$ depends on the specific model that is used to describe the data. In imaging, the signal consists of photons that are

Nature Methods: doi:10.1038/nmeth.2396

typically assumed to be detected according to a Poisson process, and all data models we consider therefore have this in common. Their differences are due to their respective image detectors, which differ in terms of noise sources and the presence or absence of pixelation.

Ultimate limit of accuracy. For the ideal data model wherein the image detector contributes no noise of any kind and is unpixelated, the Fisher information matrix for an image of a point source, where $\theta = (x_0, y_0)$ and where photons are assumed to be detected at a constant rate, can be derived from more general results[4] and written as

$$\mathbf{I}(\theta) = N_{photon}^2 \int_C \frac{1}{N_{photon} f_\theta(x,y) + \beta b(x,y)} \left(\frac{\partial f_\theta(x,y)}{\partial \theta} \right)^T \frac{\partial f_\theta(x,y)}{\partial \theta} \, dxdy, \tag{S2}$$

where C is the finite region in $\mathbb{R}^2$ occupied by the unpixelated detector, N_{photon} is the mean of the Poisson-distributed number of photons detected from the point source, f_θ is the Airy point spread function-based spatial probability density function given by equation (2), β is the mean of the Poisson-distributed number of detected background photons, and $b(x,y)$ is the probability density function describing the spatial distribution of the background photons, assumed in this paper to be uniform and given by $b(x,y) = \frac{1}{A}, (x,y) \in C$, where A is the area of C. Note that the quantity N_{photon} is the average number of point source photons detected in the entire detector plane (i.e., $\mathbb{R}^2$), and the average number detected within the finite area of the detector is therefore smaller than N_{photon}. However, in the analysis of our simulated and experimental data, regions of interest are chosen which include a large percentage of N_{photon}. Furthermore, the density function f_θ is exactly as defined by equation (2). The subscript θ is used here only to explicitly denote the dependence of f on the parameter vector θ. Note also that limits of the localization accuracy computed by assuming this ideal data model are referred to as *ultimate limits of accuracy* (**Supplementary Note 4**).

Practical limits of accuracy - effects of detector pixelation and noise. For the CCD and EMCCD data models which entail a practical imaging detector that introduces noise and is pixelated, or for data models which entail a hypothetical noiseless but pixelated detector, the Fisher information

Nature Methods: doi:10.1038/nmeth.2396

matrix for a K-pixel image of a point source is given by the general expression[5]

$$\mathbf{I}(\theta) = \sum_{k=1}^{K} \left(\frac{\partial \nu_{\theta,k}}{\partial \theta} \right)^T \frac{\partial \nu_{\theta,k}}{\partial \theta} \cdot E\left[\left(\frac{\partial}{\partial \nu_{\theta,k}} \ln(p_{\theta,k}(z)) \right)^2 \right], \tag{S3}$$

where $\nu_{\theta,k} > 0$ is given by equation (3) and represents the mean of the Poisson random variable that models the detected signal at the kth pixel of the detector, and $p_{\theta,k}(z)$ is the probability distribution of the data z at the kth pixel, and it is a function of $\nu_{\theta,k}$. Note that $\nu_{\theta,k}$ is exactly as defined by equation (3). The subscript θ is again used here to explicitly denote the dependence of ν_k on the parameter vector θ.

The definition of $p_{\theta,k}(z)$, $k = 1, \ldots, K$, depends on the data model. For a hypothetical detector that introduces no noise, for example, the data at the kth pixel consists of just the signal detected at the kth pixel, and $p_{\theta,k}(z)$ is simply the Poisson probability mass function with mean $\nu_{\theta,k}$, i.e.,

$$p_{\theta,k}(z) = \frac{e^{-\nu_{\theta,k}} \nu_{\theta,k}^z}{z!}, \quad z = 0, 1, \ldots. \tag{S4}$$

This data model is important in that it gives the benchmark limit of accuracy for the approach to UAIM that splits the detected photons over multiple images (see **Supplementary Note 8** and **Fig. S5**). Furthermore, it is used to compute limits of accuracy that are based on the common supposition that the best parameter estimation accuracy achievable with an EMCCD detector is a factor of $\sqrt{2}$ worse than the best accuracy that is achievable with a noiseless but pixelated detector. Such an excess noise-based limit of accuracy (see **Figs. 2b** and **S5**) is simply computed as $\sqrt{2}$ multiplied by the limit of accuracy corresponding to this data model.

For the CCD data model, $p_{\theta,k}(z)$ is the probability density function of the sum of the Poisson signal at the kth pixel and a Gaussian random variable that models the CCD detector's readout noise at the kth pixel, given by[1]

$$p_{\theta,k}(z) = \frac{1}{\sqrt{2\pi}\sigma_k} \sum_{j=0}^{\infty} \frac{e^{-\nu_{\theta,k}} \nu_{\theta,k}^j}{j!} e^{-\frac{1}{2}\left(\frac{z-j-\eta_k}{\sigma_k}\right)^2}, \quad z \in \mathbb{R}, \tag{S5}$$

Nature Methods: doi:10.1038/nmeth.2396

where η_k and σ_k are respectively the mean and standard deviation of the Gaussian random variable.

For the EMCCD data model, $p_{\theta,k}(z)$ is the probability density function of the sum of the amplified Poisson signal at the kth pixel and a Gaussian random variable that models the EMCCD detector's readout noise at the kth pixel, given by equation (4). The EMCCD data model is used to describe both conventional EMCCD data and UAIM data.

Supplementary Note 4: Limit of accuracy terminology

The terminology *ultimate limit of accuracy* as used in this paper in the context of point source localization, refers to the best possible accuracy that is obtainable with a hypothetical noiseless and unpixelated detector with a finite area for photon detection. In keeping with the terminology developed in our previous publications, however, it is more formally referred to as the *finite detector fundamental localization accuracy measure*, or *finite detector FLAM*, since the terminology *fundamental localization accuracy measure (FLAM)*[6] refers to the best possible accuracy that is obtainable under the similar hypothetical scenario of imaging with a noiseless and unpixelated detector, but one with an infinite area for photon detection. To be more precise, since strictly speaking the terminology FLAM assumes the detected photons to originate only from the point source, the ultimate limit of accuracy considered in this paper is a special version of the finite detector FLAM that assumes the detection of background photons (see equation (S2)) in addition to the photons from the point source.

Similarly, the terminology *limit of accuracy* as used in this paper in the context of point source localization to refer to the best possible accuracy that is obtainable under the UAIM or conventional EMCCD imaging scenario, is more formally referred to as the *practical localization accuracy measure (PLAM)*[6]. PLAM refers to the best possible accuracy that is obtainable under a practical scenario where the imaging is carried out using a pixelated detector that introduces noise and has a finite area for photon detection.

Nature Methods: doi:10.1038/nmeth.2396

Supplementary Note 5: Results of stationary single molecule data analysis

To facilitate the comparison of the localization accuracy between UAIM and conventional EMCCD imaging, four stationary Atto647N data sets were chosen for analysis such that there were two pairs of UAIM/conventional EMCCD data sets with similar mean photon counts (72.09 and 191.35 for the two UAIM data sets, and correspondingly, 84.00 and 182.96 for the two conventional EMCCD data sets). Note that the UAIM (conventional EMCCD) image shown in **Figure 1a** was taken from the UAIM data set with the 72.09 mean photon count (the conventional data set with the 84.00 mean photon count). For the digital representation shown, the image was adjusted linearly using the *immultiply* function of the MATLAB image processing toolbox.

The results of the maximum likelihood localizations are summarized in **Supplementary Table 1**. As in the case of the results of our bead data analysis, UAIM is shown to yield substantially better localization accuracies than conventional imaging. Comparing the UAIM data set with the mean photon count of 191.35 with the conventional data set with the mean photon count of 182.96, for example, **Supplementary Table 1** shows that the standard deviations of the x_0 and y_0 estimates for UAIM are essentially half of that for conventional EMCCD imaging. In both cases, the standard deviations are reasonably close to their respective limits of the localization accuracy, whose values affirm that better performance by a factor of 2 can be expected for UAIM. Importantly, only in the case of UAIM is the limit of the localization accuracy very close to (less than 2 nm from) the corresponding ultimate limit of accuracy, demonstrating that the standard deviation is itself close to the absolute best accuracy that can be expected. Note that for the pair of lower photon count UAIM and conventional data sets, a similar twofold difference in performance would also be expected if their mean photon counts and background photon counts were more closely matched as in the case of the pair of higher photon count data sets.

Nature Methods: doi:10.1038/nmeth.2396

Supplementary Note 6: The pixel photon count reduction principle of UAIM

Forming the basis of UAIM is the fact that when an EMCCD detector is operated at a high level of signal amplification (i.e., electron multiplication), the signal in a pixel is least corrupted by detector noise when less than one photon on average is detected in the pixel. The data in such a pixel therefore contains nearly as much information about the imaged object as an uncorrupted signal of the same magnitude. Extending this result to an image, it is reasonable to expect that by ensuring a high information content for each of the pixels that comprise an image of the object of interest, the resulting image will contain nearly as much information about the object as an image that is free of detector noise, and will hence enable estimation of the quantities of interest with very high accuracies. UAIM thus stipulates the reduction of the signal level per pixel to less than one photon on average, and as we have shown using the problem of point source localization as an example (see **Fig. 2b**), it does in fact allow the ultrahigh accuracy estimation of positional coordinates.

Utilizing the material presented in **Supplementary Note 3**, we demonstrate here the rationale behind the reduction of the signal level in a pixel. We make use of the *noise coefficient*[5], a number with a value between 0 and 1 that quantifies the extent to which the signal in a pixel is corrupted by detector noise (or, equivalently, the amount of information the data in a pixel contains about the quantities of interest). The noise coefficient is derived from the Fisher information matrix for the data in a pixel, and we begin by describing how it is obtained, and by providing the explicit mathematical expressions it takes on for the data models considered in this paper. We then use it to demonstrate the phenomenon on which UAIM relies.

The Fisher information matrix $\mathbf{I}(\theta)$ quantifies the amount of information the data contains about the parameters in θ. The larger the matrix, the greater the amount of information and the higher the accuracies with which the parameters can be estimated from the data. For a given pixel, equation (S3) shows that the Fisher information matrix for pixelated image data differs for different data models only by the expectation term $E\left[\left(\frac{\partial}{\partial \nu_\theta}\ln(p_\theta(z))\right)^2\right]$. Note that we have dropped the subscript k from

Nature Methods: doi:10.1038/nmeth.2396

$\nu_{\theta,k}$ since here we are dealing with a single arbitrary pixel. The expectation term is a nonnegative scalar, and is proportional to the amount of information the data contains about the parameters in θ.

To compare the Fisher information content of different data models (as we need to do to show that UAIM data contains nearly as much information as the pure signals from a hypothetical detector that introduces no noise), we therefore need only compare the values of their expectation terms. For a given signal level ν_θ, data that has the larger expectation term contains more information about the parameters in θ, and allows their estimation with higher accuracies.

Instead of comparing the expectation terms directly, however, it is useful to make comparisons using the noise coefficient, which is simply the expectation term normalized against the expectation term for the hypothetical best scenario of an uncorrupted Poisson signal. The expectation term for the hypothetical best scenario is $\frac{1}{\nu_\theta}$, and is obtained by taking $p_\theta(z)$ to be the Poisson probability mass function of equation (S4). The noise coefficient, which we denote by α, is then defined as

$$\alpha = \frac{E\left[\left(\frac{\partial}{\partial\nu_\theta}\ln(p_\theta(z))\right)^2\right]}{\frac{1}{\nu_\theta}} = \nu_\theta \cdot E\left[\left(\frac{\partial}{\partial\nu_\theta}\ln(p_\theta(z))\right)^2\right]. \tag{S6}$$

Comparing using the noise coefficient α provides the advantage that, for any given signal level ν_θ, we have $\alpha = 1$ for the hypothetical best scenario of a pure Poisson signal, and $0 \leq \alpha \leq 1$ for practical scenarios entailing a Poisson signal that is corrupted by detector noise[5]. To determine how close the Fisher information content of a particular data model is to that of a pure Poisson signal, we need only look at how close its noise coefficient is to 1.

By evaluating the expectation term with $p_\theta(z)$ given by the probability density function of equation (S5), the noise coefficient for the CCD data model can be shown to be

$$\alpha = \nu_\theta \cdot \left(\int_{-\infty}^{\infty} \frac{1}{p_\theta(z)} \cdot \left(\frac{1}{\sqrt{2\pi}\sigma}\sum_{j=1}^{\infty}\frac{e^{-\nu_\theta}\nu_\theta^{j-1}}{(j-1)!}e^{-\frac{1}{2}\left(\frac{z-j-\eta}{\sigma}\right)^2}\right)^2 dz - 1\right). \tag{S7}$$

Similarly, by evaluating the expectation term with $p_\theta(z)$ given by the probability density function

Nature Methods: doi:10.1038/nmeth.2396

of equation (4), the noise coefficient for the EMCCD data model can be shown to be

$$\alpha = \int_{-\infty}^{\infty} \frac{\nu_\theta \cdot e^{-2\nu_\theta}}{p_\theta(z)} \left(\sum_{l=1}^{\infty} \frac{e^{-\left(\frac{z-l-\eta}{\sqrt{2}\sigma}\right)^2}}{\sqrt{2\pi}\sigma g} \sum_{j=0}^{l-1} \frac{\binom{l-1}{j} \left(1-\frac{1}{g}\right)^{l-j-1}}{j! \left(\frac{g}{\nu_\theta}\right)^j} \right)^2 dz - \nu_\theta. \tag{S8}$$

Note that in equations (S7) and (S8), the subscript k has been dropped from η_k and σ_k, the mean and standard deviation of the Gaussian random variable that models the detector's readout noise. As in the case of $\nu_{\theta,k}$, the subscript k is meaningless here since we are looking at a single arbitrary pixel.

The EMCCD noise coefficient of equation (S8) is shown in **Figure S1** as a function of the mean photon count ν_θ in a pixel. The plot clearly shows that when an EMCCD detector is used at a high level of signal amplification ($g = 1000$), the noise coefficient is closest to 1 over a long mean photon count range where less than one photon on average is detected in a pixel. Therefore, at very low signal levels, the information content of the data in an EMCCD pixel is closest to that of a pure Poisson signal of the same level. UAIM exploits this phenomenon by applying it to every pixel of a region of interest (ROI), thereby enabling parameter estimation with accuracies that are close to that which would only be possible if each pixel contained a pure signal.

Note also that **Figure S1** suggests that as the mean photon count ν_θ is increased in a pixel, the EMCCD noise coefficient converges to 0.5. This indicates that at relatively high signal levels, the information content of the data in an EMCCD pixel is only half of that of a pure signal. As we showed previously[5], this halving of the information content can be related to the well-known excess noise factor[7,8,9] that results from the stochastic nature of signal amplification. Based on this factor, it is commonly supposed that the standard deviation for estimating a parameter from an EMCCD image is at best $\sqrt{2}$ times the standard deviation that is attainable with a hypothetical noiseless detector. **Figure S1** importantly demonstrates, however, that the $\sqrt{2}$ penalty applies only at relatively high signal levels, and that significantly less penalty is incurred at very low signal levels.

For comparison, the CCD noise coefficient of equation (S7) is also shown in **Figure S1** for the same range of mean photon counts. This plot illustrates two important points. First, the fact that the noise coefficient approaches 1 with increasing photon count demonstrates the suitability of the

Nature Methods: doi:10.1038/nmeth.2396

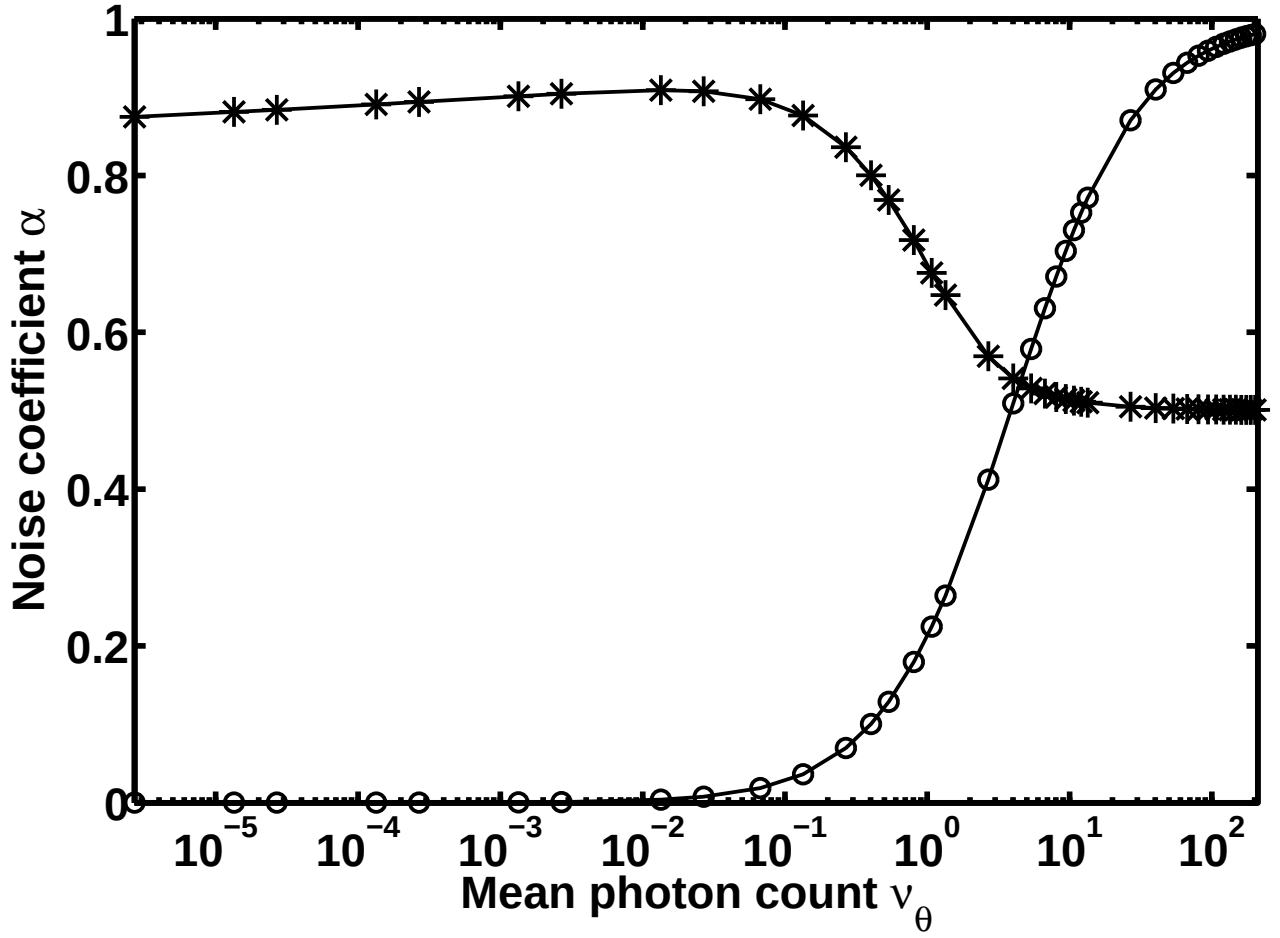

Figure S1. Noise coefficient as a function of the expected photon count in a pixel. Reducing the signal level in a pixel to less than one photon on average in an EMCCD camera operated at a high level of signal amplification ($g = 1000$) ensures that the detected signal is minimally deteriorated by detector noise. This is shown by the noise coefficient ($*$) being closest to 1 over a long range of mean photon counts that are less than one. In sharp contrast, the noise coefficient for a CCD camera ($\circ$) is closest to 0 at the same low signal levels. For the EMCCD scenario, the mean and the standard deviation of the readout noise are set to $\eta = 0$ electrons and $\sigma = 24$ electrons. For the CCD scenario, they are set to $\eta = 0$ electrons and $\sigma = 2$ electrons.

Nature Methods: doi:10.1038/nmeth.2396

CCD detector when enough light is available. Second, the small values of the noise coefficient at low photon counts, and the near-zero values at very low photon counts, show that even with a low readout noise of $\sigma = 2$ electrons, the CCD detector is unsuitable for extreme low light imaging and for implementing UAIM. Plotting the CCD noise coefficient curve additionally shows the crossover point from the EMCCD regime to the CCD regime, which occurs approximately at a mean photon count of 4.5 in the pixel. For mean photon counts higher than 4.5, using a CCD detector is more beneficial than using an EMCCD detector in terms of the estimation accuracies that can be expected. Note however that this crossover point pertains to an electron multiplication gain of 1000 and a readout noise standard deviation of 24 electrons for the EMCCD detector, and a readout noise standard deviation of 2 electrons for the CCD detector. In the ensuing discussion, the effects that an EMCCD detector's electron multiplication gain and readout noise level have on the value of the EMCCD noise coefficient (and hence the crossover point between the EMCCD and CCD regimes) will be examined.

Effects of electron multiplication gain and readout noise. **Figure S1** shows the EMCCD noise coefficient for values of the electron multiplication gain ($g = 1000$) and the readout noise ($\sigma = 24$ electrons) that are typical of currently available EMCCD detectors. Our theory shows that by increasing the electron multiplication gain and/or decreasing the readout noise level, however, the noise coefficient can be even closer to 1 at the very low signal levels. **Figure S2**, for example, illustrates the effect of the electron multiplication gain by showing the noise coefficient curves for the same conditions as in **Figure S1**, but with electron multiplication gains ranging from 5 to 5000. The figure shows that whereas the noise coefficient curve for a gain of 1000 tops out at nearly 0.91 at the very low signal levels, the curve for a gain of 2000 tops out at nearly 0.95, and the curve for a gain of 5000 easily exceeds 0.95 throughout most of the low signal range, reaching as high as nearly 0.98. On the other hand, **Figure S2** shows that as the electron multiplication gain is decreased, the noise coefficient values are also decreased. Arbitrarily picking 0.6 as the minimally acceptable noise coefficient value, the figure shows that for a readout noise level of 24 electrons, electron multiplication gains of 100 or below should probably not be used, with the curve for the gain of 100 topping out at just under 0.6 at

Nature Methods: doi:10.1038/nmeth.2396

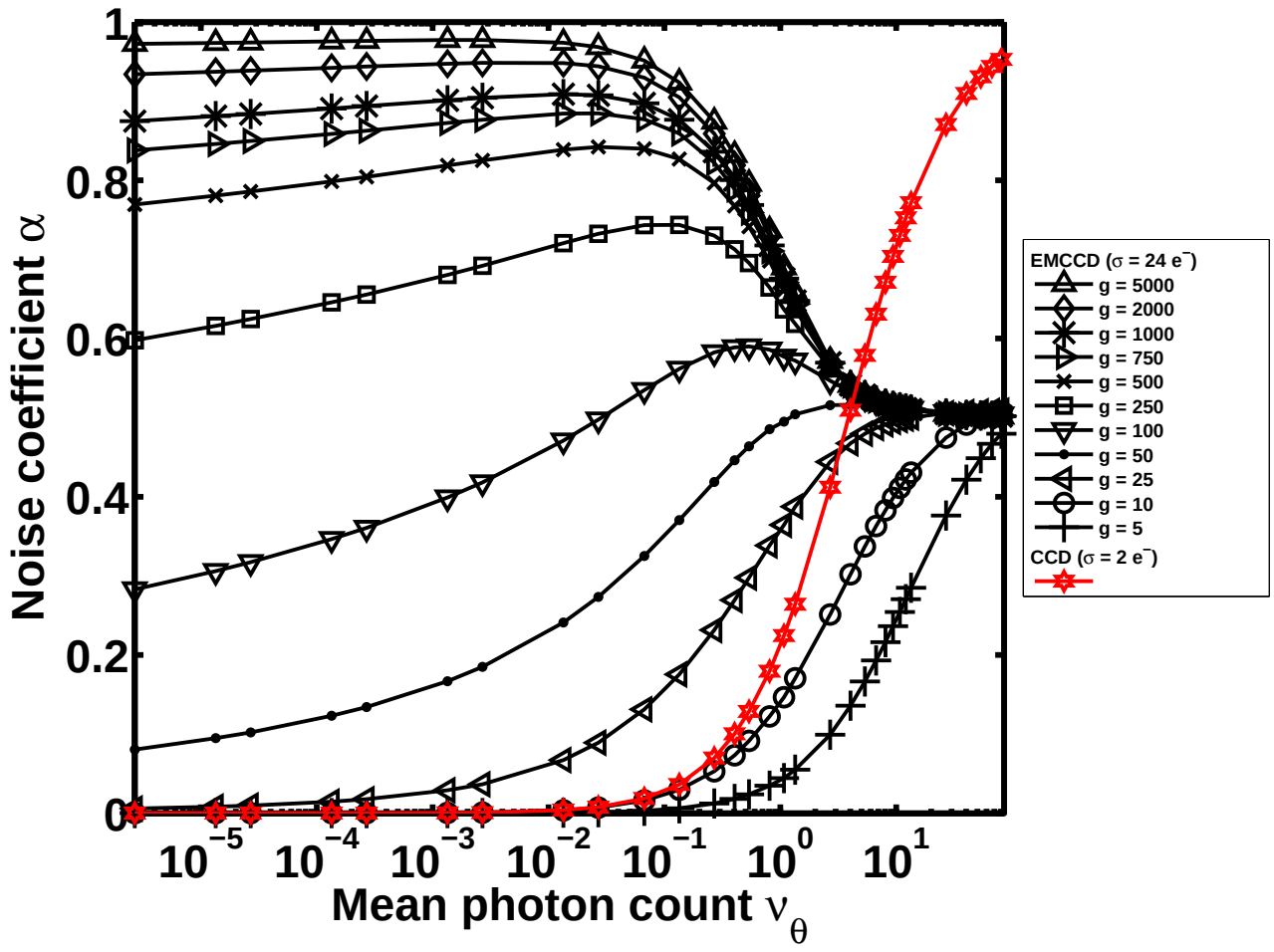

Figure S2. EMCCD noise coefficient for values of the electron multiplication gain ranging from $g = 5$ to $g = 5000$, and a readout noise standard deviation of $\sigma = 24$ electrons. For a given mean photon count in the low signal range, the value of the noise coefficient is shown to improve (i.e., increase) with increasing gain. The CCD noise coefficient (red curve) for a readout noise standard deviation of $\sigma = 2$ electrons is also shown for comparison. The mean of the readout noise is set to $\eta = 0$ electrons in all cases.

a mean photon count of around 0.5 photons. Instead, gains of 250 or above should be used, as their noise coefficients are at least 0.6 throughout the very low photon count range shown.

In terms of the crossover point between the EMCCD and CCD regimes, **Figure S2** shows that for electron multiplication gains ranging from 5000 to a relatively low 250, the crossover points are essentially the same at approximately 4.5 photons. For a gain of 100, the crossover point is only slightly

Nature Methods: doi:10.1038/nmeth.2396

lower at around 4.4 photons. For gains of 50 and 25, the crossover points occur at approximately 4.1 and 3.2 photons, respectively, and for the very low gains of 10 and 5, the crossover points occur at very low mean photon counts (less than 1 by at least a couple orders of magnitude). In fact, the curve for a gain of 5 is smaller than the CCD noise coefficient curve throughout the entire range of photon counts shown. The results for the gain values of 10 and 5 demonstrate the impracticality of using the EMCCD detector at very low gain levels where the amplified signals are too weak to be distinguished from the readout noise.

To demonstrate the effect of the readout noise, **Figure S3** shows the same noise coefficient curves as in **Figure S2**, but with the standard deviation of the readout noise increased threefold to $\sigma = 72$ electrons. The figure shows that a higher readout noise level results in a downward shift of each curve, indicating as expected that the signal in the pixel is more corrupted by detector noise for the same gain values. The curves for electron multiplication gains of 1000, 2000, and 5000, for example, are now below 0.8, 0.9, and 0.95, respectively, throughout the entire range of photon counts shown. Applying the same arbitrary criterion of a minimum noise coefficient value of 0.6 as before, **Figure S3** shows that for a readout noise level of 72 electrons, one should use an electron multiplication gain of at least 750.

Figure S3 further shows that, despite the increased readout noise, the crossover point between the EMCCD and CCD regimes remains relatively unchanged at around 4.5 photons for electron multiplication gains of 500 and higher, and drops slightly to around 4.3 photons for a gain of 250. The crossover point drops more significantly, however, to about 3.7 photons and 1.7 photons for gains of 100 and 50, respectively, and the curves for gains of 25 and 10 join the curve for a gain of 5 as being completely below the CCD curve throughout the entire range of photon counts shown. The general trend of a lower crossover point for a given gain (compared to the corresponding curve in **Fig. S2**) is expected, since the increased readout noise makes it more difficult, at a given gain, to distinguish an amplified signal from the readout noise.

Finally, the noise coefficient curves of **Figure S4** show that when used at an electron multiplication gain of 1000 (representative of the maximum gain of an Andor iXon EMCCD camera), the EMCCD

Nature Methods: doi:10.1038/nmeth.2396

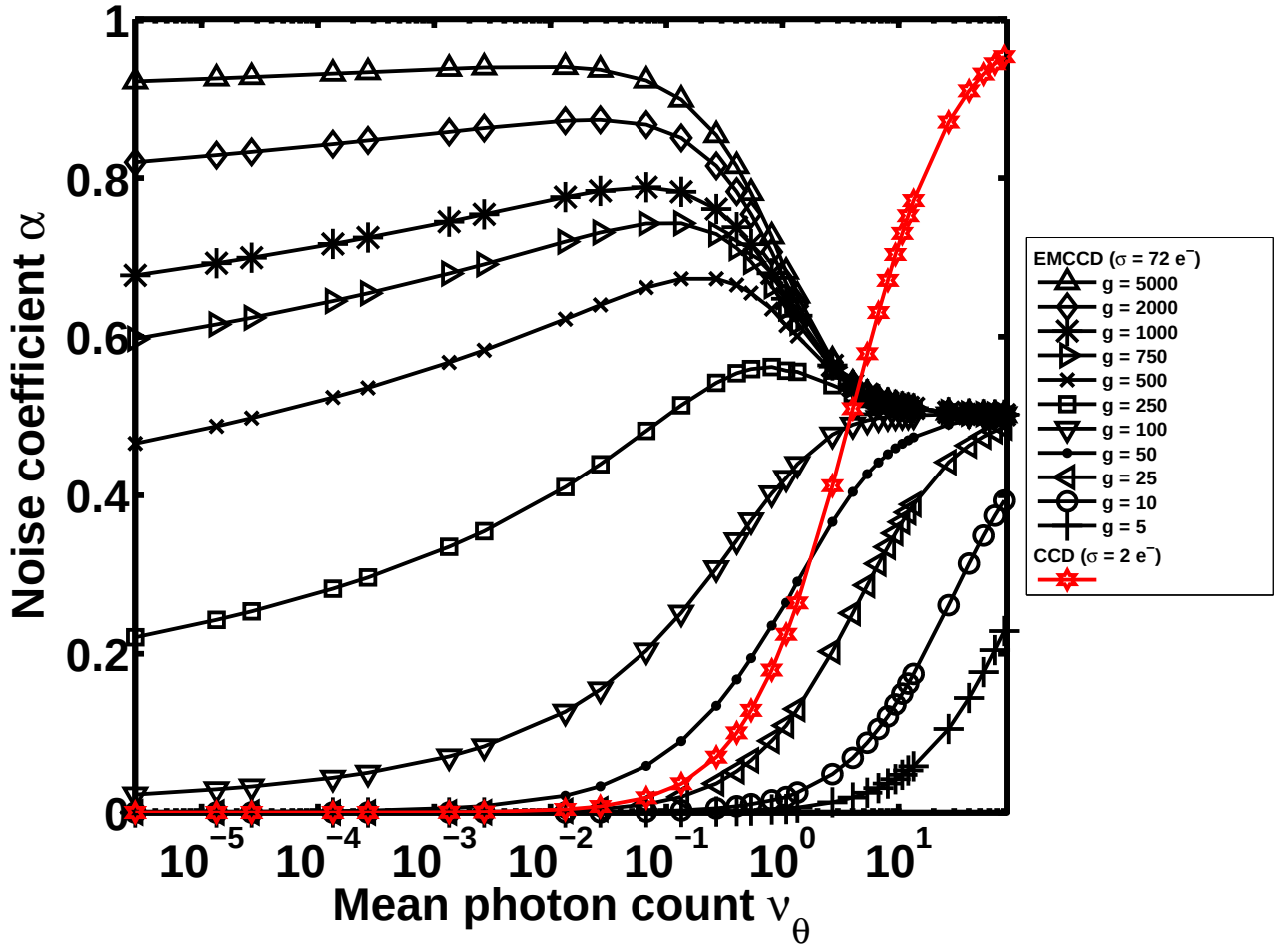

Figure S3. EMCCD noise coefficient for values of the electron multiplication gain ranging from $g = 5$ to $g = 5000$, and a readout noise standard deviation of $\sigma = 72$ electrons. Compared to **Figure S2**, the noise coefficient curves have lower values in the low photon count range due to the increased readout noise. The CCD noise coefficient (red curve) for a readout noise standard deviation of $\sigma = 2$ electrons is again shown for comparison. The mean of the readout noise is set to $\eta = 0$ electrons in all cases.

Nature Methods: doi:10.1038/nmeth.2396

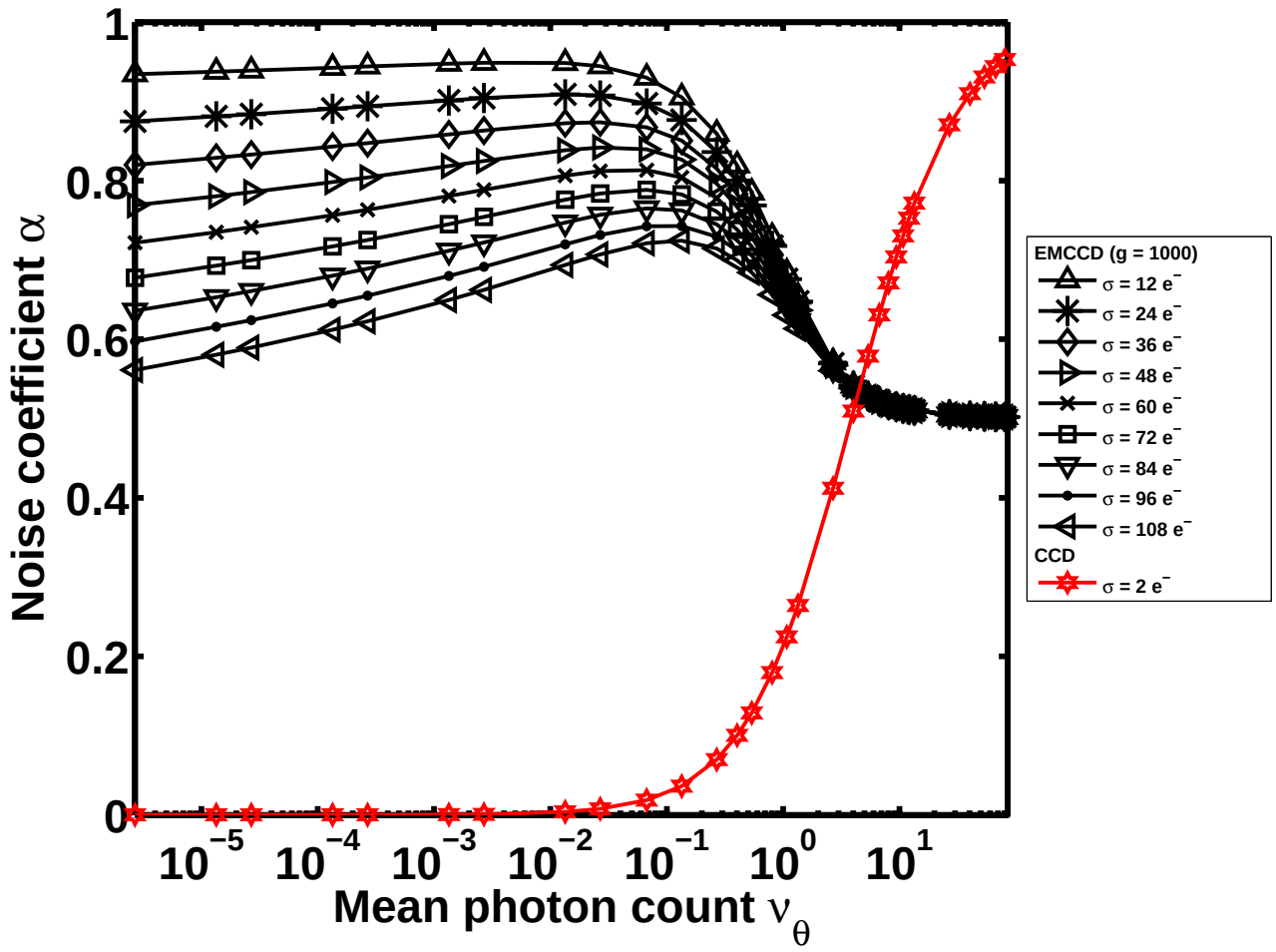

Figure S4. EMCCD noise coefficient for readout noise standard deviations ranging from $\sigma = 12$ electrons to $\sigma = 108$ electrons, and an electron multiplication gain of $g = 1000$. The CCD noise coefficient (red curve) for a readout noise standard deviation of $\sigma = 2$ electrons is shown for comparison. The mean of the readout noise is set to $\eta = 0$ electrons in all cases.

Nature Methods: doi:10.1038/nmeth.2396

detector provides significant benefit throughout the low photon count range shown for readout noise standard deviations of 12 to 108 electrons. Specifically, though the value of the noise coefficient decreases as expected with increasing readout noise for a given mean photon count, the minimum noise coefficient value of the lowest curve (σ = 108 electrons) is 0.56 in the low photon count range, approximately meeting the arbitrary minimum criterion value of 0.6. Since the chosen range of standard deviations encompasses the readout noise levels associated with the various readout modes of a typical Andor iXon camera, **Figure S4** demonstrates that when operated at maximum electron multiplication gain, any readout mode of a typical Andor iXon can be used to achieve a significant level of benefit that is inversely proportional to the readout noise standard deviation.

Supplementary Note 7: Overcoming the reduction of field of view

While the use of high magnification to implement the pixel size reduction approach to UAIM necessarily reduces the field of view, it does not preclude UAIM from being used as a practical imaging method. There are different ways to increase the field of view, one of which is to use an EMCCD detector that yields a larger field of view at the same effective pixel size. Andor's iXon3 888 camera, for example, has a 1024×1024-pixel detector with a 13 μm pixel size which requires an 812.5$\times$ magnification to get to the same 16 nm effective pixel size of our bead, tracking, stationary single molecule, and LAMP1$^+$ cellular structure superresolution data. At this effective pixel size, the available field of view is 16.384 μm $\times$ 16.384 μm, or four times larger than the 8.192 μm $\times$ 8.192 μm field of view obtained with the 512×512-pixel, 16 μm pixel detector of the Andor iXon camera that we used with a 1000$\times$ magnification. Importantly, it should be noted that even with the smaller 8.192 μm $\times$ 8.192 μm total field of view, we were able to use less than half of it (a 200×512-pixel area) to perform the superresolution imaging of an entire cellular structure (**Fig. 1b**). Furthermore, we were able to use the entire 8.192 μm $\times$ 8.192 μm field of view to track the movement of a single dye molecule for over 60 seconds (**Fig. 1c** and **Supplementary Video 1**).

A second way to implement UAIM with a larger field of view is to use a smaller magnification. Rather than using a 1000$\times$ magnification, for example, we have demonstrated superresolution imaging

Nature Methods: doi:10.1038/nmeth.2396

at a 630× magnification, where the field of view (an approximately 13 μm × 13 μm area) contains an entire biological cell (**Supplementary Fig. 3**). Importantly, despite the bigger effective pixel size of approximately 25.4 nm, not much localization accuracy is lost. Compared to the limit of accuracy of 23.36 nm for localizing the average molecule (**Supplementary Note 15**) had the imaging been performed at 1000×, the limit of accuracy for the 630× imaging is 25.32 nm, or only worse by 1.96 nm. Moreover, the accuracy limit of 25.32 nm is still much closer to the ultimate accuracy limit of 20.32 nm, compared to the limit of accuracy of 38.72 nm had the imaging been carried out with conventional EMCCD imaging at a 63× magnification (see **Supplementary Table 3**). Note that the fact that a smaller magnification in the vicinity of 630× yields a worse, but comparable accuracy compared to a magnification in the vicinity of 1000× can also be seen (for a different set of experimental parameters) in **Figure 2b**. There, the limit of accuracy at a similar magnification of 700× is shown to be 6.96 nm, compared to 6.74 nm for 1100×.

A third way to realize UAIM with a larger field of view is to image different small fields of view (sequentially using a single camera or simultaneously using multiple cameras) and stitch them together to yield a large field of view. This is a commonly used technique for imaging large biological samples, and software tools[10] are available for stitching the acquired images.

Note that the field of view issue pertains to the pixel size reduction approach to UAIM, and that other approaches to UAIM are possible that do not decrease the field of view. As detailed in **Supplementary Note 8**, for example, UAIM can be realized by acquiring, at a standard magnification, many dim (e.g., underexposed) images in lieu of a single relatively bright image. Though this approach to UAIM does not provide as big of an accuracy improvement (since it does not increase the image resolution by producing a more finely pixelated image), **Figure S5** shows that it can still yield a significant accuracy advantage over conventional EMCCD imaging.

It is also important to note that it is possible to have a larger field of view by realizing UAIM via a combination of approaches. Take for example the accuracy of 8.25 nm attained at a 242.86× magnification in **Figure 2b**. If one wanted to improve the accuracy to 7.24 nm (i.e., to get even closer to the ultimate limit of 6.19 nm) while keeping the same magnification (and hence the same relatively

Nature Methods: doi:10.1038/nmeth.2396

large field of view of approximately 33.73 μm $\times$ 33.73 μm (assuming a 512 $\times$ 512-pixel, 16 μm pixel detector), which is almost 17 times larger than the field of view at 1000$\times$), one could incorporate the approach of **Supplementary Note 8** by acquiring at the 242.86$\times$ magnification 50 underexposed images, each having a mean photon count of 4, to obtain a mean total photon count of 200. This is as opposed to acquiring a single image with a mean photon count of 200 at a 500$\times$ magnification, which gives a similar accuracy of 7.21 nm, but at the cost of a field of view that is about 4 times smaller.

Supplementary Note 8: A different approach to implementing UAIM

Instead of reducing the (effective) pixel size of the EMCCD detector, a different approach to realizing UAIM is to split the photons that would normally be detected in a single image over multiple images, such that generally less than one photon on average is detected in a given pixel of any image. To obtain a single estimate of the quantity of interest, maximum likelihood estimation is then carried out on an entire set of the resulting dim images that correspond to a single normally acquired and relatively bright image. To demonstrate this approach to UAIM, **Figure S5** shows that when using an EMCCD detector at a high level of signal amplification, the limit of the accuracy for localizing a point source improves as one decreases the mean photon count detected per image (and accordingly, increases the number of dim images used to obtain a single positional coordinate estimate). In fact, the figure shows that one can get close to 8.56 nm, the best possible accuracy that is only attainable with a noiseless detector with the same pixelation. For example, whereas analyzing one image with an expected photon count of 200 (i.e., conventional EMCCD imaging) gives a best possible accuracy of 11.72 nm, analyzing a set of 1000 images each with an expected photon count of just 0.2 yields a best possible accuracy of 8.99 nm, which is within half a nanometer of the 8.56 nm limit.

Nature Methods: doi:10.1038/nmeth.2396

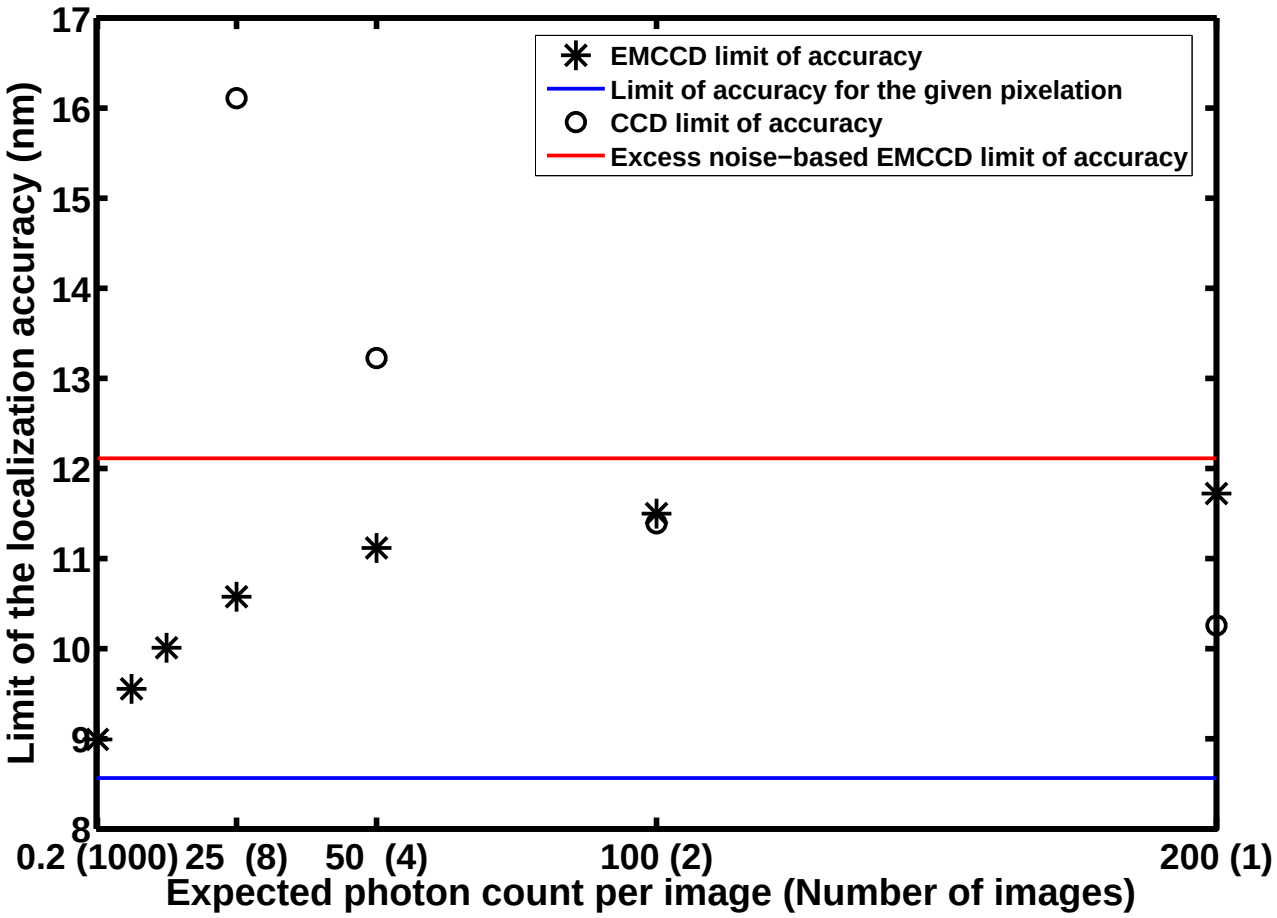

Nature Methods: doi:10.1038/nmeth.2396

Figure S5. Implementing UAIM by acquiring many dim images instead of a single relatively bright image. Cutting down the expected number of photons detected per image by, for example, reducing the exposure time for EMCCD imaging at a high level of signal amplification ($g = 1000$), and performing the parameter estimation on sets of underexposed images rather than individual normally exposed images, yield a limit of the localization accuracy ($*$) that approaches the limit that is attainable only with a noiseless detector with the same pixelation (blue line). The plot shows limits of accuracy for configurations ranging from 1 image with a mean photon count of 200, to 1000 images with a mean photon count of 0.2 per image. Each configuration is constructed such that a total of $N_{photon} = 200$ photons on average are detected at the detector plane over the entire set of underexposed images. For comparison, the plot also shows the limit of the localization accuracy (red line) that is calculated based on the common assertion that the best estimation accuracy attainable with an EMCCD detector is worse than that which is achievable with a noiseless but pixelated detector by a factor of $\sqrt{2}$. Furthermore, to demonstrate that UAIM cannot be achieved with a CCD camera, even one with a low level of readout noise, the limits of the localization accuracy ($\circ$) corresponding to CCD imaging with a mean of $\eta_k = 0$ electrons and a small standard deviation of $\sigma_k = 2$ electrons for the readout noise at each pixel k are also shown for the same configurations. In all cases, the limits of accuracy pertain to the localization of an in-focus point source whose image as observed through the microscope is described by the Airy point spread function. The magnification and numerical aperture of the objective lens are respectively set to $M = 100$ and $n_a = 1.3$, and the wavelength of the photons is set to $\lambda = 655$ nm. It is assumed that the image formed is exactly centered on the square region that is used in the localization. Specifically, the region of interest is a 7×7 array of 16 μm $\times$ 16 μm pixels, which captures 183.33 out of the expected 200 photons for the entire detector plane and over the entire set of underexposed images. No background component is assumed, and its mean is accordingly set to $\beta_k = 0$ photons for each pixel k. For the EMCCD scenario, the mean and the standard deviation of the readout noise are respectively set to $\eta_k = 0$ electrons and $\sigma_k = 24$ electrons for each pixel k. (Note that since its image is exactly centered on a square region of interest, the limits of accuracy shown pertain to both the x_0 and y_0 coordinates of the point source.)

Note that the benchmark limit of 8.56 nm here is worse than the ultimate limit of 6.19 nm (see **Fig. 2b**) that serves as the target for the effective pixel size reduction approach to UAIM. This is due to the retention of the relatively coarse pixelation of the detector. By distributing the detected photons over multiple images, the current approach only minimizes the deteriorative effect of the detector noise in each pixel of the acquired images. It does not alter the effective pixel size to produce a more finely resolved image, and therefore does nothing to lessen the deteriorative effect of the coarse pixelation.

Figure S5 also shows the limit of accuracy corresponding to the common excess noise-based supposition that the best parameter estimation accuracy achievable with an EMCCD detector is a factor of $\sqrt{2}$ worse than what is attainable with a noiseless but pixelated detector. Comparing this

Nature Methods: doi:10.1038/nmeth.2396

limit (12.11 nm) with the limits for the EMCCD scenario, our plot clearly shows that it makes a reasonable approximation (to 11.72 nm) at an expected 200 photons per image when the mean signal per pixel is relatively high. However, the approximation deteriorates as the expected photon count per image decreases, and in fact becomes a very poor one when the mean photon count per image is reduced to just 0.2. At that point, the approximation significantly underestimates the attainable accuracy of 8.99 nm, which is again within half a nanometer of the best limit.

Finally, to illustrate the unsuitability of a CCD detector, even one with a low level of readout noise, for implementing this alternative approach to UAIM, **Figure S5** also shows the limits of accuracy for the same imaging conditions, but assuming the use of a CCD detector with a readout noise standard deviation of only 2 electrons. For this scenario, the best possible accuracy is seen to worsen significantly, rather than improve, as the expected photon count per image is decreased.

It is important to note that different approaches to UAIM are not mutually exclusive. See **Supplementary Note 7** for an example of combining the approach presented here with the pixel size reduction approach.

Supplementary Note 9: Parameters for the theoretical analysis of pixel size reduction

In all scenarios shown in **Figure 2b**, the limits of the localization accuracy (**Supplementary Note 3**) pertain to the localization of an in-focus point source whose image as observed through the microscope is described by the Airy point spread function. The numerical aperture of the objective lens is set to $n_a = 1.3$, and it is assumed that an average of $N_{photon} = 200$ point source photons of wavelength $\lambda = 655$ nm are detected per image at the detector plane. It is further assumed that the image formed is exactly centered on the square ROI that is used in the localization. For the EMCCD, CCD, and noiseless but pixelated detector-based (i.e., excess noise-based) scenarios, the ROI for the 160.00 nm effective pixel size ($M = 100$) is a 7×7 array of 16 μm $\times$ 16 μm pixels (i.e., number of pixels $K = 49$, and for $k = 1, \ldots, K$, the region C_k over which the integral of equation (3) is evaluated is set to the 16

Nature Methods: doi:10.1038/nmeth.2396

μm $\times$ 16 μm region occupied by pixel k), which captures an expected 183.33 point source photons out of the 200 total expected point source photons per image. For each of the other effective pixel sizes, the ROI is a proportionally reduced or expanded region (e.g., 21×21 array of 16 μm $\times$ 16 μm pixels for the effective pixel size of 53.33 nm ($M = 300$)) to ensure the same 183.33 expected number of detected photons. For the ideal scenario, the ROI C for each effective pixel size is the same as that for its counterparts in the other scenarios, but is unpixelated and therefore records the location of each detected photon with arbitrarily high precision. As the limit of accuracy for the ideal scenario (i.e., the ultimate limit of accuracy) is the same regardless of the effective pixel size, it is simply shown as a continuous horizontal line. For the EMCCD scenario, the signal amplification level is set to $g = 1000$, and the mean and standard deviation of the readout noise are respectively set to $\eta_k = 0$ electrons and $\sigma_k = 24$ electrons for each pixel k. For the CCD scenario, the mean and standard deviation of the readout noise are respectively set to $\eta_k = 0$ electrons and $\sigma_k = 2$ electrons for each pixel k. For all scenarios, no background component is assumed, and its mean is accordingly set to $\beta = 0$ photons for the ideal scenario, and $\beta_k = 0$ photons for each pixel k for the EMCCD, CCD, and noiseless but pixelated detector-based scenarios. (Note that since its image is exactly centered on a square ROI, the limits of accuracy shown pertain to both the x_0 and y_0 coordinates of the point source.)

Supplementary Note 10: UAIM versus sCMOS imaging

Since an image acquired with a complementary metal oxide semiconductor (CMOS) detector can be modeled in the same way as an image acquired with a CCD detector, the results shown in this paper for the CCD detector apply equally well to a CMOS detector with the same parameters (i.e., pixel size, readout noise level, etc.). **Figure 2b** therefore shows that the CMOS detector is also unsuitable for implementing UAIM.

Recently, scientific CMOS (sCMOS) detectors with per pixel readout noise standard deviations as low as 1 electron have become available. Imaging using these new detectors, for example, has been demonstrated and compared with conventional EMCCD imaging in the context of superresolution microscopy[11]. To demonstrate that the sCMOS detectors do not outperform UAIM, we show in

Nature Methods: doi:10.1038/nmeth.2396

Supplementary Figure 1a essentially the same plot as in **Figure 2b**, but with limits of accuracy included which correspond to an sCMOS detector with $\sigma_k = 1$ electron for all pixels k. Additionally, limits of accuracy are plotted which correspond to a hypothetical sCMOS detector with an even better readout noise level of $\sigma_k = 0.5$ electrons for all pixels k. The figure shows that whereas UAIM produces limits of accuracy that approach the ultimate limit of 6.19 nm, the sCMOS limits of accuracy given a per pixel readout noise level of 1 electron are approximately no better than the 8.92 nm achieved at an effective pixel size of 124.45 nm. The hypothetical sCMOS detector with a per pixel readout noise level of 0.5 electrons performs better, but still only attains approximately a best limit of accuracy of 7.88 nm at the effective pixel size of 86.16 nm. Furthermore, note that **Supplementary Figure 1a** assumes an expected photon count of 200 from the point source, and that the advantage that UAIM has over the sCMOS (and CCD) detectors can be expected to widen as the expected photon count decreases (i.e., as the readout noise of the sCMOS detector becomes more significant). This is illustrated by **Supplementary Figure 1b**, which assumes an expected photon count of 50 from the point source and shows a significantly wider gap between the limits of accuracy that are achievable with UAIM and the sCMOS (and CCD) detectors.

Supplementary Note 11: UAIM at different photon budgets

The principle of UAIM is applicable regardless of the number of photons that are detected from the object of interest. Given any photon budget, reducing the photon count in each pixel of an EMCCD detector (operated at a high level of signal amplification) to the low signal range shown in **Figure S1** will in principle yield a significant improvement in the estimation accuracy. To demonstrate this, limits of the accuracy (i.e., theoretical best possible standard deviations; see **Supplementary Note 3**) for localizing a point source have been computed by assuming the conditions of **Figure 2b**, but for mean photon counts ranging from 200 to 3200 per image of the point source. The limits of accuracy for UAIM have been calculated assuming the high magnification implementation of the pixel size reduction approach to UAIM.

The results are summarized in **Supplementary Table 2** where for each photon count, limits of

Nature Methods: doi:10.1038/nmeth.2396

accuracy are shown for imaging with an ideal (i.e., noiseless and unpixelated) detector, conventional EMCCD imaging at a 100× magnification, UAIM at a 900× magnification, UAIM at a 4500× magnification, and CCD imaging with a low readout noise standard deviation of 2 electrons. For the CCD scenario, the accuracy limit for a given photon count was computed at a near-optimal magnification (i.e., a magnification that yields approximately the best accuracy limit) for that photon count. For each of the four practical imaging scenarios, the distance between its limit of accuracy and its corresponding ultimate limit of accuracy (i.e., accuracy for the ideal imaging scenario) is expressed as a percentage (in square brackets) of the ultimate limit of accuracy. The smaller this percentage, the closer the limit of accuracy is to its corresponding ultimate limit of accuracy.

A comparison of the numbers in **Supplementary Table 2** for conventional EMCCD imaging and UAIM at 900× shows that UAIM yields a significant advantage over conventional imaging for all five photon counts considered. For the conventional EMCCD accuracy limit, the distance from the ultimate accuracy limit is large, ranging from 89.3% for a mean photon count of 200 to 94.8% for a mean photon count of 3200. In sharp contrast, for UAIM at 900×, the distance from the ultimate limit is much smaller, ranging from 10.0% for a mean photon count of 200 to 22.6% for a mean photon count of 3200.

If implemented at an even higher magnification of 4500× to further reduce the photon count in each pixel, **Supplementary Table 2** shows that the accuracy limit for UAIM improves further to about 6% from the ultimate limit for all five photon counts considered. Note however that practically, if the reduction of the field of view by a factor of 25 when going from a 900× to a 4500× magnification is a concern, one might choose the 900× implementation at the cost of a relatively small loss of accuracy. For example, even for the mean photon count of 3200 where the most improvement is gained by choosing the higher magnification (distance from the ultimate limit decreases from 22.6% to 6.5%), the accuracy limit of 1.90 nm at 900×, compared to 1.65 nm at 4500×, might be acceptable. However, if the difference is important, then one might choose the 4500× magnification and consider ways to increase the field of view such as those suggested in **Supplementary Note 7**.

It is well-known[2] that conventional imaging with a CCD detector can yield high localization

Nature Methods: doi:10.1038/nmeth.2396

accuracies when enough photons are detected to render the detector's readout noise insignificant. This result can be seen in **Supplementary Table 2**, where for the CCD limit of accuracy, the distance from the ultimate accuracy limit improves from 65.8% for a mean photon count of 200 to 29.7% for a mean photon count of 3200. Nevertheless, it can be seen that both UAIM at 900× and UAIM at 4500×, with distances of 22.6% and 6.5%, respectively, still have the advantage at the highest photon count of 3200. The accuracy difference between UAIM and CCD imaging, however, clearly narrows with increasing photon count. Therefore, at relatively high photon counts like 1600 and 3200, one might consider the tradeoff between the better estimation accuracy enabled by UAIM and the larger field of view of conventional CCD imaging. Given the near-optimal magnification of 185.7× used for the photon count of 3200, for example, the field of view for the CCD scenario is about 23.5 times larger than that for UAIM at 900×. However, if the higher accuracy offered by UAIM is critical, then one might choose UAIM and again consider the suggestions in **Supplementary Note 7** for increasing the field of view.

Note that for UAIM at 900×, some pixels in the image have a mean photon count that is greater than 1 when the mean total photon count from the point source is 400 or higher. For example, when the mean total photon count from the point source is 3200, almost 13% of the pixels in the 63×63-pixel ROI have a mean photon count greater than 1, and the brightest pixel has a mean photon count of 12.49. As explained in **Supplementary Note 1**, this does not violate the principle of UAIM, which recommends but does not require the number of photons detected in each pixel of an image to be less than one on average. Indeed, even with pixels that detect more than 1 photon on average, **Supplementary Table 2** shows the substantial advantage of UAIM at 900× over conventional EMCCD imaging for mean total photon counts of 400 and higher.

Supplementary Note 12: Parameters for the simulated data sets

For each imaging scenario of **Table 1**, 1000 images of a point source were simulated. The images were simulated by assuming the point source to emit photons of wavelength $\lambda = 655$ nm, and the objective lens to have a numerical aperture of $n_a = 1.3$. The expected number of point source photons

Nature Methods: doi:10.1038/nmeth.2396

detected per image at the detector plane was set to $N_{photon} = 200$, and the image of the point source was assumed to be given by the Airy point spread function. For the ideal scenario, the magnification was set to $M = 100$, and the Airy function was centered on a 112 μm $\times$ 112 μm unpixelated ROI C. For the conventional EMCCD scenario, the same magnification of $M = 100$ was used and the Airy function was centered on a region of the same size, but consisting of a 7×7 array of 16 μm $\times$ 16 μm pixels (i.e., number of pixels $K = 49$, and for $k = 1, \ldots, K$, the region C_k over which the integral of equation (3) is evaluated was set to the 16 μm $\times$ 16 μm region occupied by pixel k). The effective pixel size was therefore 160 nm. This produced images where the brightest pixel had a relatively high mean photon count of 53.48. For the UAIM scenario, the magnification was increased ninefold to $M = 900$, and the Airy function was centered on an accordingly expanded 63×63 array of 16 μm $\times$ 16 μm pixels. The effective pixel size was therefore 17.78 nm. This produced images where the brightest pixel had a small mean photon count of only 0.78. The described ROIs capture an expected 183.33 point source photons out of the 200 total expected point source photons per image. For the conventional EMCCD and UAIM scenarios, the mean and standard deviation of the detector readout noise were respectively set to $\eta_k = 0$ electrons and $\sigma_k = 24$ electrons for each pixel k, and a signal amplification level of $g = 1000$ was assumed. For all scenarios, no background component was assumed, and its mean was accordingly set to $\beta = 0$ photons for the ideal scenario, and $\beta_k = 0$ photons for each pixel k for the conventional EMCCD and UAIM scenarios.

Supplementary Note 13: Camera acquisition parameters

For all data sets, the Andor iXon camera was operated in frame transfer mode, and the baseline clamp was used. The electron multiplication gain was set to 950, and the pre-amplifier gain was set to 5.0$\times$. The 1 $\times$ 1 binning mode was used, and the camera temperature was set to -70°C. The vertical shift speed was set to 0.5 μs.

For all bead data sets, the readout mode used was 1 MHz 16 bit. For the conventional (UAIM) bead data sets, a 64 $\times$ 64-pixel area (128 $\times$ 128-pixel area) was continuously acquired at an exposure time of 37.8 ms (73.2 ms).

Nature Methods: doi:10.1038/nmeth.2396

For the LAMP1$^+$ cellular structure (cell membrane) superresolution data set, the readout mode used was 3 MHz 14 bit, and a 200 $\times$ 512-pixel area (512 $\times$ 512-pixel area) was continuously acquired at an exposure time of 41 ms (105 ms).

For the live cell single molecule tracking data set, the readout mode used was 3 MHz 14 bit, and a 512 $\times$ 512-pixel area was continuously acquired at an exposure time of 101 ms. For all stationary single molecule data sets, the readout mode used was 5 MHz 14 bit. For the conventional (UAIM) stationary single molecule data sets, a 256 $\times$ 384-pixel area (512 $\times$ 512-pixel area) was continuously acquired at an exposure time of 40 ms (101 ms).

Supplementary Note 14: Fixed parameters for the experimental data sets

For a given localization of a bead or single molecule, parameters other than x_0 and y_0 were set or determined as follows, and used in the maximum likelihood estimation of x_0 and y_0 as fixed values. The parameter M in equation (2) was set to the value of the magnification at which the image was acquired, and the parameter g in equation (7) was set to 950, the value of the electron multiplication gain at which the Andor iXon camera was operated. The parameter K in equation (6) was set to the number of pixels comprising the square ROI on which the image of the bead or single molecule was approximately centered. For each (Andor iXon) pixel k in the ROI, the region C_k over which the integral of equation (3) is evaluated was set to the 16 μm $\times$ 16 μm region occupied by the pixel. For each pixel k, the readout noise mean η_k in equation (7) was set to 0 electrons, since the camera offset was subtracted from the ROI. The standard deviation of the readout noise, assumed to be the same for all pixels in the ROI, was given by the standard deviation of the pixel values of a sequence of small, minimally exposed images acquired using the same readout mode as the experimental data, but with the camera shutter closed and the electron multiplication gain set to the lowest value possible. For each pixel k, the readout noise standard deviation σ_k in equation (7) was determined to be 19.2 electrons for the bead data sets, 40.9 electrons for the stationary single molecule data sets, and 30.6 electrons

Nature Methods: doi:10.1038/nmeth.2396

for the live cell single molecule tracking data set, the LAMP1$^+$ cellular structure superresolution data set, and the cell membrane superresolution data set. The different readout noise standard deviations are due to the use of different camera readout modes (**Supplementary Note 13**) to acquire the data sets.

The value of the width parameter (i.e., the term $\frac{2\pi n_a}{\lambda}$ in equation (1)) of the Airy point spread function was determined as follows for the different data sets. For the localization accuracy comparison studies where many repeat images were acquired of a given bead or stationary Atto647N molecule, the ROIs from the individual repeat images were added to produce a sum ROI. The width parameter for the given bead or Atto647N molecule was then obtained by fitting an Airy point spread function to the sum ROI using nonlinear least squares estimation that was implemented with the *lsqnonlin* function of the MATLAB optimization toolbox. The subsequent maximum likelihood localization of each bead or stationary Atto647N molecule was performed using its own value for the width parameter that was determined in this way. For the 10 (11) conventional EMCCD (UAIM) bead data sets presented in **Figure 2a** and **Supplementary Figure 2**, the average value of their width parameters is 0.00713 nm^{-1} (0.01263 nm^{-1}). For each of the four stationary Atto647N data sets that were analyzed, the value of its width parameter is given in **Supplementary Table 1**.

For the LAMP1$^+$ cellular structure and cell membrane superresolution data sets, no repeat images of the same Alexa647 molecule were available. However, in each case, width estimation using the same sum ROI method was applied to data sets consisting of repeat images of stationary Alexa647 molecules that were acquired using the same microscope and imaging setup as the superresolution data set. The width parameter for the superresolution data set was then taken to be the average of the width estimates obtained for several different stationary Alexa647 molecules. For the LAMP1$^+$ cellular structure (cell membrane) data set, the value of the width parameter was determined to be 0.01056 nm^{-1} (0.00951 nm^{-1}), and was used in the maximum likelihood localization of all Alexa647 molecules analyzed in the superresolution data set. For the live cell single molecule tracking data set, the same strategy for width estimation was applied, but using data sets consisting of repeat images of stationary Atto647N molecules. The value of the width parameter was determined to be 0.01034

nm^{-1}, and was used in the maximum likelihood localization of the tracked Atto647N molecule in each track frame of the tracking data set.

The expected number of photons detected per image from a bead or single molecule (i.e., N_{photon} in equation (3)), and the expected number of background photons detected per pixel in the ROI (i.e., β_k in equation (3), assumed to be the same for each pixel k), were determined as follows for the different data sets. For the localization accuracy comparison studies using beads or stationary Atto647N molecules, N_{photon} and β_k for the given bead or Atto647N molecule were obtained from the equivalent parameters for the sum ROI which were simultaneously estimated with the width parameter. Specifically, N_{photon} and β_k were determined by dividing the nonlinear least squares estimates of the equivalent parameters by the number of individual ROIs forming the sum ROI, and by the electron multiplication gain of 950. The subsequent maximum likelihood localization of each bead or stationary Atto647N molecule was performed using its own values for N_{photon} and β_k that were determined in this way. For the 10 (11) conventional EMCCD (UAIM) bead data sets that were analyzed, their values for N_{photon} are used as the independent variable in **Figure 2a** and **Supplementary Figure 2**, and the average value of their expected per-pixel background photon count β_k is 3.34 photons (0.032 photons). For each of the four stationary Atto647N data sets that were analyzed, the values for N_{photon} and β_k are given in **Supplementary Table 1**.

For the LAMP1$^+$ cellular structure and cell membrane superresolution data sets, the N_{photon} and β_k parameters were determined using ROIs extracted from the compacted (i.e., 10×10 binned) version of the data sets. For a given Alexa647 molecule, a photon count estimate and a per-pixel background estimate were obtained by fitting an Airy point spread function to its ROI, which resembled the image of a molecule acquired at a standard magnification. The fitting was carried out using nonlinear least squares estimation where the width parameter was fixed to the value determined as described above. The resulting photon count estimate was then divided by the electron multiplication gain of 950 to obtain the value for N_{photon}. The per-pixel background estimate was similarly divided by 950, but also further divided by 100 to account for the image compaction, to obtain the value for β_k. For the Alexa647 molecules that were eventually used to construct the superresolution image, the average

Nature Methods: doi:10.1038/nmeth.2396

value of N_{photon} (β_k) is 128.94 (0.18) photons for the LAMP1$^+$ cellular structure data set, and 233.94 (0.91) photons for the cell membrane data set.

For the live cell single molecule tracking data set, the N_{photon} and β_k parameters were similarly determined for the tracked Atto647N molecule in each track frame using the compacted version of the data set. The average value of N_{photon} for the tracked Atto647N molecule over the 594 track frames is 102.85 photons, and the average value of β_k is 0.086 photons.

Supplementary Note 15: Limit of accuracy calculations for the data sets

For the localization accuracy comparison studies using beads and stationary Atto647N molecules, limits of the accuracy for estimating the x_0 and y_0 coordinates of a given bead or Atto647N molecule were computed with x_0 and y_0 respectively given by the mean of the (drift-corrected) x_0 and y_0 maximum likelihood estimates, and with the other parameters given by the same fixed values (**Supplementary Note 14**) as used in the maximum likelihood estimation. Specifically, limits of accuracy corresponding to the EMCCD data model and the ideal data model were computed as described in **Supplementary Note 3**, and are shown in the plots of **Figure 2a** and **Supplementary Figure 2** for the bead data sets, and in **Supplementary Table 1** for the stationary Atto647N data sets, for comparison with the standard deviations of the x_0 and y_0 maximum likelihood estimates. For the ideal data model (i.e., the ultimate limit of accuracy), the integral of equation (S2) was evaluated over a continuous area of the same size as the ROI. Also, the mean background photon count β was set to the total mean background photon count in the ROI (i.e., the mean per-pixel background photon count β_k multiplied by the number of pixels K in the ROI).

For the LAMP1$^+$ cellular structure and cell membrane superresolution data sets, limits of the localization accuracy were computed (according to the EMCCD data model) for the *average* Alexa647 molecule to characterize the accuracy with which the x_0 and y_0 coordinates of the activated Alexa647 molecules were determined using maximum likelihood estimation. The average molecule is taken to

Nature Methods: doi:10.1038/nmeth.2396

be one whose image is perfectly centered in the 50 × 50-pixel ROI that was used for the maximum likelihood localizations, and whose expected photon count N_{photon} and expected per-pixel background photon count β_k are the averages of the N_{photon} and β_k parameters (**Supplementary Note 14**) for the Alexa647 molecules that were used in the construction of the superresolution image. All other parameters required by the calculation of the limit were given by the same fixed values as used in the maximum likelihood localizations.

To see what the localization accuracy would in theory have been for the average molecule had conventional EMCCD imaging been used to carry out the same experiment, the limit of accuracy was also calculated for all the same conditions, but for a 5 × 5-pixel ROI and a magnification that is ten times smaller. Additionally, the ultimate limit of accuracy was computed (according to the ideal data model) for the given conditions. All the computed limits of accuracy are given in **Supplementary Table 3** for both the LAMP1$^+$ cellular structure data set and the cell membrane data set.

For the live cell single molecule tracking data set, limits of accuracy were computed in similar fashion as described for the superresolution data sets, but for the *average image* of the tracked Atto647N molecule. The average image is one where the image of the Atto647N molecule is perfectly centered in the 50 × 50-pixel ROI that was used for the maximum likelihood localization in each track frame, and where the expected photon count N_{photon} and expected per-pixel background photon count β_k are the averages of the N_{photon} and β_k parameters (**Supplementary Note 14**) for the tracked Atto647N molecule over the 594 track frames. The computed limits of accuracy are given in **Supplementary Table 3**.

For the simulated data sets of **Table 1**, limits of accuracy were computed using the parameter values with which the data was simulated (see **Supplementary Note 12**).

Nature Methods: doi:10.1038/nmeth.2396

References

[1] Snyder, D. L., Helstrom, C. W., Lanterman, A. D., Faisal, M. & White, R. L. Compensation for readout noise in CCD images. *J. Opt. Soc. Am. A* **12**, 272–283 (1995).

[2] Ober, R. J., Ram, S. & Ward, E. S. Localization accuracy in single molecule microscopy. *Biophys. J.* **86**, 1185–1200 (2004).

[3] Rao, C. R. *Linear statistical inference and its applications* (Wiley, 1965).

[4] Ram, S., Ward, E. S. & Ober, R. J. A stochastic analysis of performance limits for optical microscopes. *Multidimens. Syst. Signal Process.* **17**, 27–57 (2006).

[5] Chao, J., Ward, E. S. & Ober, R. J. Fisher information matrix for branching processes with application to electron-multiplying charge-coupled devices. *Multidimens. Syst. Signal Process.* **23**, 349–379 (2012).

[6] Abraham, A. V., Ram, S., Chao, J., Ward, E. S. & Ober, R. J. Quantitative study of single molecule location estimation techniques. *Opt. Express* **17**, 23352–23373 (2009).

[7] Matsuo, K., Teich, M. C. & Saleh, B. E. A. Noise properties and time response of the staircase avalanche photodiode. *IEEE Trans. Electron Devices* **32**, 2615–2623 (1985).

[8] Hollenhorst, J. N. A theory of multiplication noise. *IEEE Trans. Electron Devices* **37**, 781–788 (1990).

[9] Hynecek, J. & Nishiwaki, T. Excess noise and other important characteristics of low light level imaging using charge multiplying CCDs. *IEEE Trans. Electron Devices* **50**, 239–245 (2003).

[10] Schindelin, J. et al. Fiji: an open-source platform for biological-image analysis. *Nat. Methods* **9**, 676–682 (2012).

[11] Huang, Z. et al. Localization-based super-resolution microscopy with an sCMOS camera. *Opt. Express* **19**, 19156–19168 (2011).

Nature Methods: doi:10.1038/nmeth.2396